Journal of ELECTRONIC MATERIALS, Vol. 47, No. 11, 2018
https://doi.org/10.1007/s11664-018-6591-0
© 2018 The Minerals, Metals & Materials Society

Needle-Like La-Doped MgO Photocatalyst: Synthesis, Characterization and Photodegradation of Flumequine Antibiotic Under UV Irradiation

ALI İMRAN VAIZOĞULLAR [1,2]

1.—Medical Services and Techniques Department, Vocational School of Health Services, Muğla Sıtkı Koçman University, Menteşe 48000, Muğla, Turkey. 2.—e-mail: aliimran@mu.edu.tr

La-doped MgO samples with different La content were prepared via a sol–gel method using magnesium nitrate hexahydrate and Lanthanum nitrate. The prepared samples were characterized by scanning electron microscopy (SEM), x-ray photoelectron spectroscopy (XPS), x-ray diffraction (XRD), photoluminescence (PL) and UV–visible diffuse reflectance spectroscopy (UV–Vis DRS). The influence of La^{+3} in the MgO structure was investigated against Flumequine (FLQ) photodegradation. SEM images displayed needle-like MgO crystals, whereas the addition of La^{+3} decreased the needle's length. This study concludes that an optimal amount of La^{+3} can remarkably increase the photocatalytic performance of MgO. These results have been attributed to the crystalline defect.

Key words: La-doped, MgO, flumequine, crystallite defect, photocatalysis

INTRODUCTION

The development of the pharmaceutical industry has improved human health at the price of increased environmental pollution. There are various methods to deal with organic pollutants, but recently, the photocatalytic degradation of drugs such as antibiotics, anticonvulsants, antipyretics, cytostatic drugs, and different hormones has garnered significant attention in the literature.[1] Following metabolism, a drug enters the environment in the form of other organic molecules[2] that are potentially harmful. Some researchers have focused on the degradation of antibiotics by the normal flora; however, this method increases sensitivity towards bacterial infections. Antibiotics can cause allergic reactions and give rise to antibiotic-resistant bacteria. This resistance could be transferred to other aquatic media.[3] Adsorption,[4] catalytic oxidation,[5] advanced oxidation processes,[6] membrane filtration biodegradation, and electrochemical treatment,[7] among other strategies, are widely used to decompose toxic organic compounds. Among these methods, semiconductor photocatalysis has been widely used to remove phenol-based pollutants from wastewater.

Recently, the preparation of metal oxides e.g., magnesium oxide (MgO) having different physicochemical properties has been used in variety of applications.[8,9] MgO has been reported as a nontoxic thermal and electrical insulator, with high adsorption ability and antimicrobial properties. Most importantly, it exhibits high photocatalytic performance due to its large surface area to volume ratio.[10] These properties, therefore, justify its use in broader applications such as water treatment, catalysis, and bactericide.[11,12] Rare earth metals play an important role in advanced oxidation processes due to their electronic transitions between 4f–5d and 4f–4f orbitals.[13] The f orbital of the lanthanides enables complexation with amines, aldehydes, and alcohols. This property allows for efficient adsorption of the organic pollutants onto the catalyst surface. In addition, rare earth metals could contribute to the cracking of hydrocarbons when used as a dopant.[14] Therefore, in the last decade, there has been a growing trend towards the

(Received April 11, 2018; accepted August 7, 2018; published online August 21, 2018)

use of La-doped $TiO_2$and ZnO materials, among others, in the photocatalytic degradation of organic contaminants due to their efficient separation of electron–hole pairs under UV or visible light. To the best of our knowledge, while some researchers have reported the use of La-doped TiO_2, ZnO, $BiFeO_3$, BiOBr, and other materials, La-doped MgO for photocatalytic investigations has not been reported in the literature.

Herein, we report the catalytic activity of La-doped MgO against Flumequine (FLQ) antibiotic as a model pollutant. The results obtained in this study demonstrate that La-doped MgO has superior photocatalytic performance than pure MgO alone. Also, the mechanism of the photocatalytic degradation of Flumequine (FLQ) using La-Doped MgO under UV light is discussed in detail.

EXPERIMENTAL

Preparation of MgO and La-Doped MgO

All reagents were of analytical grade. First, (x) mol of magnesium nitrate hexahydrate $Mg(NO_3).6H_2O$ and Lanthanum chloride 7-hydrate ($LaCl_3.7H_2O$) were dissolved in 100 mL of H_2O; samples with x equal to 0 mol, 0.03 mol, 0.06 mol, 0.12 mol and 0.18 mol were denoted MgO, 1La-MgO, 2La-MgO, 4La-MgO, and 6La-MgO, respectively. 10 mL of citric acid was added to this solution, and it was stirred for 60 min. Next, 17 mL of ammonia solution (NH_3OH) was added. The mixture was dried at 90°C for 120 min and calcined at 650°C for 120 min.

Characterizations

The crystalline structures were examined by x-ray diffraction (XRD: Rigaku D/MAX 350) using copper K radiation (λ = 0.154056 nm). The microstructure and shape of the particles were investigated using SEM (JEOL JSM-7600F). X-ray photoelectron spectroscopic (XPS) measurement was performed using a PHI 5000 Versa Probe. The photoluminescence (PL) emission spectra of the samples were obtained using a spectrofluorometer (Spex 500 M, USA). The UV–vis DRS analyses of all the samples were performed using a Lambda 35 UV–vis spectrophotometer in the solid state.

RESULTS AND DISCUSSIONS

SEM Analysis

Figure 1 shows the SEM images of the pure MgO and 4La-MgO samples. Both samples display uniform morphology with needle-like structures due to the aggregation of several thousand nanoparticles.[15] The addition of La^{+3} decreased the needle's length. This result may be due to the greater ionic radius of La^{+3} which provides stronger electrostatic attraction in the MgO structure. Specifically, stronger interactions pull O^{2-} atoms towards La^{+3}. Therefore, shorter needle-like particles were obtained during the synthetic process.

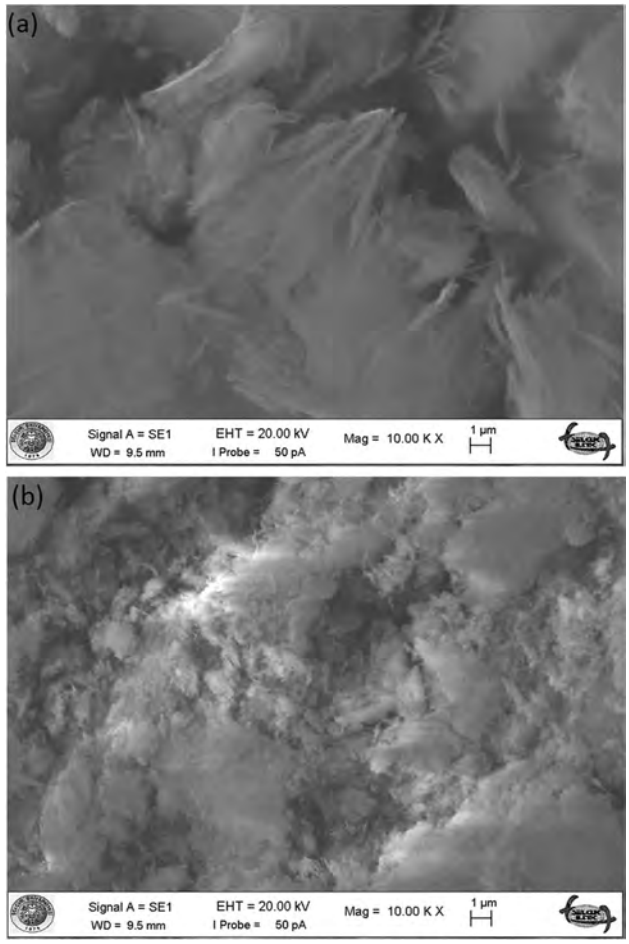

Fig. 1. SEM images of pure MgO (a) and La-doped MgO (4La-MgO sample) (b).

XRD Analysis

Figure 2 presents the XRD patterns of the synthesized particles. Pure MgO 2θ patterns were observed at 37.15°, 42.94°, 62.09°, 74.65° and 78.44° corresponding to (111), (200), (220), (311) and (222) planes, respectively, that represent the face-centered cubic structure of MgO that is consistent with the JPDS card (no. 78-0430).

The peak of the secondary La_2O_3 phase was observed in the XRD (Fig. 2a) and the peak intensity initially increased with 1 to 4% of La content, and then decreased. This confirms the efficient incorporation of MgO in the 6La-MgO sample. These findings also suggest that La^{3+} ions were efficiently dispersed on the MgO crystalline structure. Figure 2b shows that the characteristic 2θ peaks of La^{+3}-doped MgO have shifted. As is well-known, for a uniform strain, the XRD diffraction peaks exhibit a shift to high or low 2θ degree. The high-2θ shift originates from consistent compressive

stress during the low-2θ shift from a uniform tensile strain. The strain-broadening belongs to the non-uniform stress; a peak broadening can be observed without changing the peak position.[16] The peak position shifts to higher 2θ and broadening of the main 2θ peak indicate the uniform compressive strain in the composites and that La^{3+} ions have entered the crystallite structure of MgO resulting in high-quality particles. In addition, the higher peak intensity at 42.54° [(200) plane] indicates that the particle has grown along the (200) direction.[17] Broadening of the two dominant peaks at the (200) and (220) planes strongly confirms the nanocrystallinity of the MgO. The peak intensity also decreased when the amount of La^{3+} in the MgO structure increased. The average crystallite size (d_{200}) was calculated using the Scherrer Eq. 1:

$$d = \frac{B\lambda}{\beta_{1/2}\mathrm{Cos}\theta} \quad (1)$$

where d is the average crystallite size, B is the Scherrer constant (0.91), λ is the wavelength of the x-ray, $\beta_{1/2}$ is full width at half maximum of the diffraction peak and θ is the angle.[18] The dislocation density, microstrain and stacking default for La^{+3}-doped MgO were calculated using the following equations:

$$\text{Dislocation density, } \delta = \frac{1}{D^2} \quad (2)$$

$$\text{Microstrain, } \in = \frac{\beta\mathrm{Cos}\theta}{4} \quad (3)$$

$$\text{Stacking fault, SF} = \left[\frac{2\pi^2}{45(3\tan\theta)^{\frac{1}{2}}}\right]\beta \quad (4)$$

The calculated crystallite size, along with the structural and lattice parameters of MgO and La-doped MgO with different dopant concentrations, is presented in Table I. As is well known, the use of a lower ionic radius element for doping causes a constructive effect on diffusivity that results in higher crystallinity and enhanced orientation growth.[19] The ionic radius of Mg^{+2} and La^{3+} are 0.072 nm and 0.1016 nm, respectively. Therefore, doping of La^{3+} ions could inhibit the diffusion and extension of MgO particles. It can thus be suggested that with the increase of La^{3+} dopant, the crystallite size and lattice parameters of the MgO decreased.[20]

The calculated crystallite sizes of MgO and the doped samples were found to be 17.88 nm, 10.37 nm, 9.48 nm, 8.62 nm and 7.92 nm, respectively. The lattice parameters of the catalysts were significantly lower than that of MgO. A possible explanation for this, as mentioned earlier, might be that the ionic radius of Mg^{+2} is smaller than that of La^{3+} ions. Moreover, differences in the lattice parameters and shifting of the peak position (Fig. 2b) also confirms the efficient incorporation of La^{3+} ions in the MgO structure via replacement of Mg^{+2} ions. Because the radius of La^{3+} (0.1016 nm) is

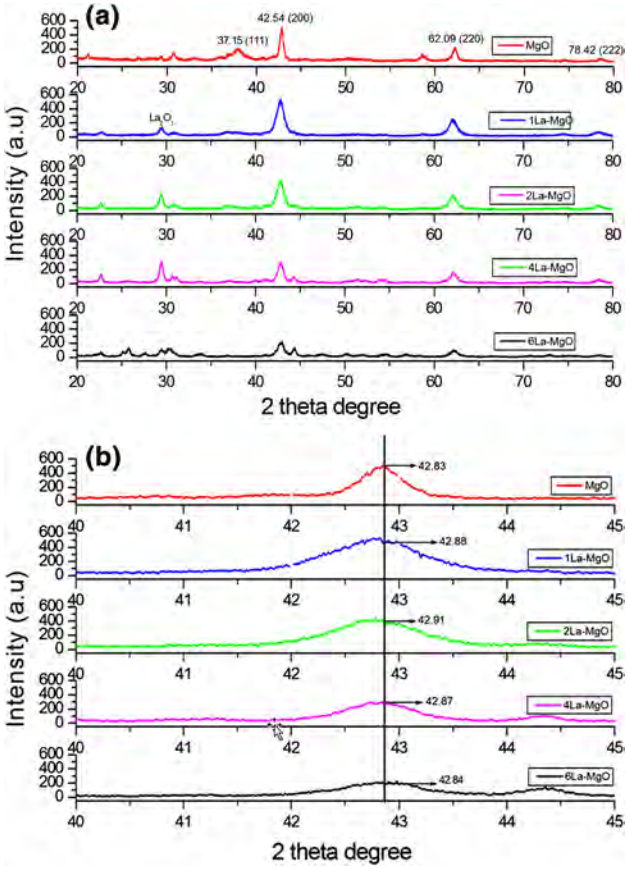

Fig. 2. XRD spectra of the samples (a) and shifting angle of the main peak of MgO (b).

Table I. The optical band gap, structural parameters and kinetic results of the samples

Sample	Crystallite size (nm)	Lattice constants (Å)	Band gap (ev)	Dislocation density (δ) × 10^{-3}	Microstrain ($\in$)	Stacking fault (SF)	Kinetic rate constant × 10^{-3} (min^{-1})	R^2
Pure MgO	17.88	4.2312	3.88	3.13	0.081	0.116	3	0.94
1La-MgO	10.37	4.2252	3.85	9.31	0.181	0.260	6.5	0.91
2La-MgO	9.48	4.2212	3.74	11.1	0.167	0.240	8	0.95
4La-MgO	8.62	4.2186	3.66	13.4	0.139	0.199	10.7	0.98
6La-MgO	7.92	4.2051	3.62	15.9	0.152	0.218	7	0.96

larger than that of Mg^{2+} (0.072 nm), when La^{3+} is doped into the MgO lattice, the La atom will remain in substitutional sites rather than interstitial spaces in the MgO structure. This incorporation in the MgO lattice decreased the crystallite size, thereby imparting excellent photocatalytic performance to MgO under UV light.

In a per unit volume of the crystal, the length of dislocation is defined as the dislocation density, which affects the properties and features of any material. Other disruptions connect the activity of a disorder. Therefore, greater dislocation density gives rise to greater hardness.[21] The dislocation density increased with doping concentration, suggesting more structural defects and lattice imperfections (Table I). The micro-strain for pure MgO and La-doped MgO samples are also given in Table I. The micro-strain was found to be higher than for La-doped samples, which can be attributed to the imperfections. However, within the doped MgO, the micro-strain decreased initially and then increased, where the amount of fault was most likely lower than the others.

Photoluminescence Analysis

The PL spectra of MgO and La-doped MgO are presented in Fig. 3a and b. Due to the structural defects, the PL properties were examined. As is known, the most common defects in the MgO crystallite structure are interstitial oxygen, oxygen vacancies, energy levels revealed in the forbidden band gap of MgO and surface states.[22] The PL spectrum was obtained at 300 nm and 400 nm. Each spectrum shows (Fig. 3a) five bands at 354 nm, 422 nm, 461 nm, 485 nm and 522 nm. In the UV region, the emission peak at 354 nm can be related to the scattering from the voids during the calcination process,[23] or free excitation recombination. The blue emission peaks at 422 nm and 461 nm can be attributed to the structural defects in the MgO, i.e., Mg vacancies and interstitials.[24]

As seen in Fig. 4a, several Gaussian fits, which show the various bands in the blue and green-yellow ranges, were observed. The green emission at 522 nm can be attributed to the acceptor level of Mg (V_{Mg}), while the emission at 507 nm is usually exhibited by an oxygen vacancy (V_o).[25] The most intense peak was observed for the 4La-MgO sample. At 400 nm, the PL spectra of the samples strictly changed and visible emission shifted towards blue-green (Fig. 3b). The highest intensity PL spectrum was obtained from the 4La-MgO sample. This confirmed that the 4La-MgO sample has more crystallite defects within the structure. It also indicates an optimum dopant concentration within the MgO lattice to initiate productive photo-induced charge transfer processes. The peaks at 558 nm and 595 nm can be described as the oxygen vacancy F-centers (O_2 particle interstices possessed by two e^-)

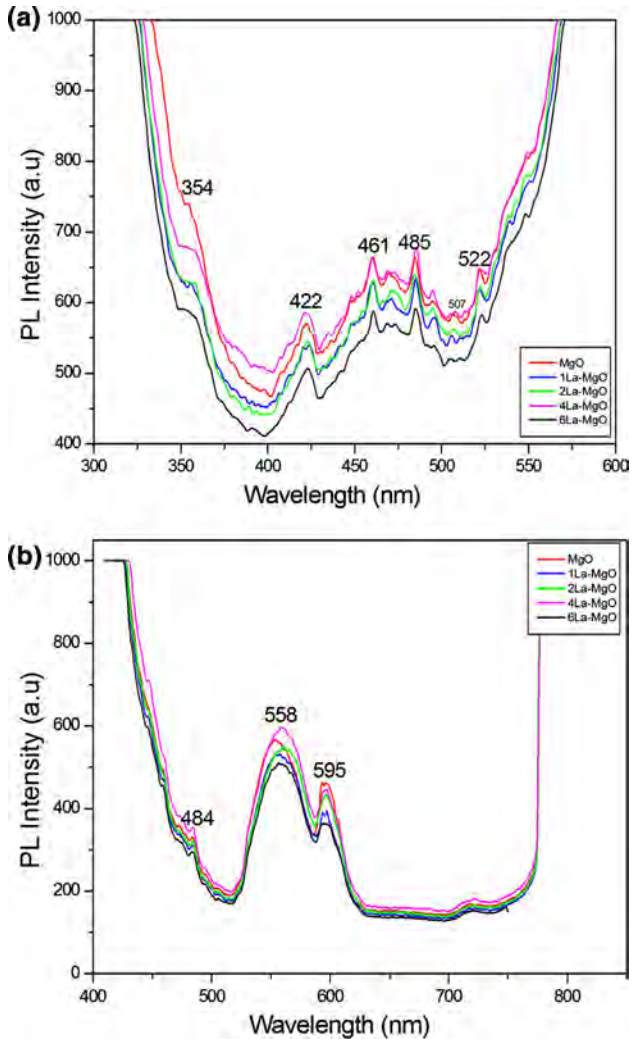

Fig. 3. PL spectra of MgO and La-doped MgO: 300 nm excitation (a) 400 nm excitation (b).

or F^+-centers (O_2 vacancy involved by single e-) or surface states.[26]

XPS Analysis

The XPS spectra of the 4La-MgO sample are shown in Fig. 4 where the Mg, O, and La^{3+} signals are visible, suggesting the presence of these elements in the 4La-MgO sample. The spectrum (Fig. 5a) confirms the significant peaks for Mg and O on the catalyst surface.[27] The central Mg KLL Auger emission peaks were observed between 304.5 eV and 307.25 eV (Fig. 5a). This confirms the polycrystalline metallic magnesium. The peak around 286.11 eV represents the C 1s due to contamination. The signal related to O1s in the high resolution can be observed as a doublet (Fig. 5b). The peak at 528.8 eV can be attributed to the lattice oxygen of MgO (OL) and other binding energies of 531.1 eV that are related to the surface defects and chemisorbed oxygen species (OA).[28] It

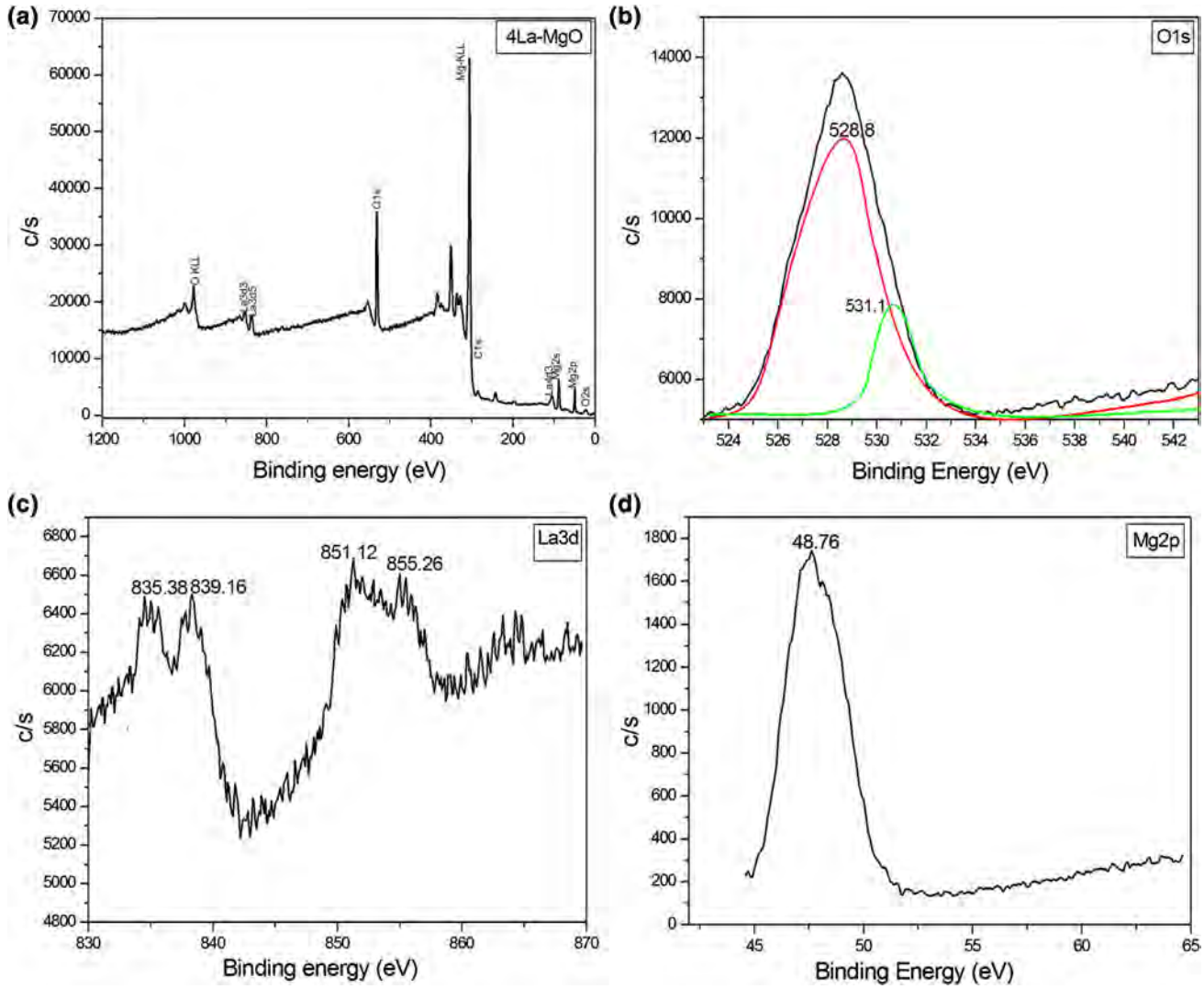

Fig. 4. XPS spectra of La-doped MgO (a) survey, (b) O 1s, (c) La3d (d) Mg2p.

can be concluded that the molar percentage of OA is too small due to the inoccupation of the interstitial sites in the MgO lattice; thus the generation of oxygen vacancies is enhanced. As seen in Fig. 5c, the doublet peaks around 835.38–839.16 eV for La $3d_{5/2}$ and 851.12–855.26 eV for La $3d_{3/2}$ were consistent with the standard binding energy of La.[20] The XPS spectrum of the Mg2p exhibits one peak at 49.61 eV that is consistent with the previous report (Fig. 5d).[29]

Optical Properties

The absorption spectra of MgO and La-doped MgO samples are shown in Fig. 5. The absorption maxima (λ_{max}) of all the catalysts were observed around 300–350 nm in the UV region. Compared to pure MgO, the absorption peak of La^{3+}-doped MgO samples reflected a red shift in the UV region that is attributed to La^{3+} impurities present within the

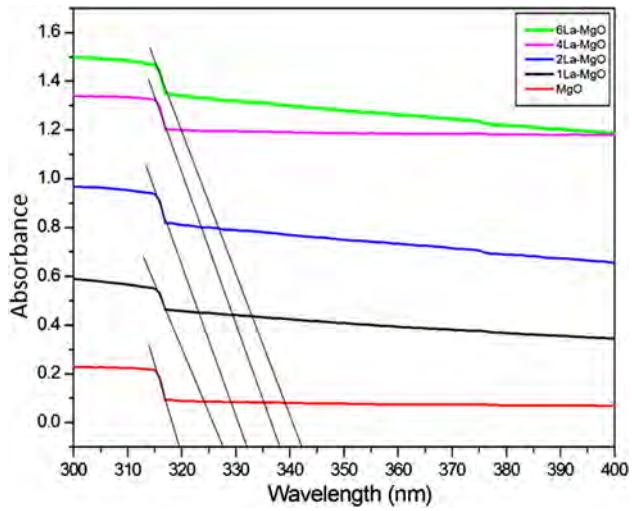

Fig. 5. The optical absorption spectra of MgO and La-doped MgO samples.

interstices of the MgO lattice. The optical band gap values of all catalysts were calculated using $E_g = \frac{1240}{\lambda}$ formula (Table I). The Eg values varied from 3.88 eV to 3.62 eV for MgO and La-doped MgO, respectively (Table I). Additionally, decreasing the band gap values related to the defects and local bond distortions, besides the intrinsic surface states, and interfaces yielded confined electronic levels within the forbidden band gap.[30] Formation of the secondary La_2O_3 phase decreased the E_g value of the doped samples. It can thus be suggested that La-doped MgO can be useful under UV light.

Photocatalytic Activity

Generally, the photocatalytic performance of a catalyst is related to the BET surface area, crystallinity, and morphology. The photocatalytic activity can be increased by expanding the separation rate of electron–hole pairs by shifting the excitation to a higher wavelength. This procedure starts with the following steps: when an electron in the valence band (VB) level of a semiconductor is excited, an electron–hole pair is generated, and this is followed by the diffusion of charge into the catalyst surface, where highly reactive species such as superoxide $(O_2^{\cdot -})$ and hydroxide radicals $(OH^{\cdot})$ form.[31] These radicals play an essential role in the degradation of organic contaminants.

The photocatalytic activity of each sample was evaluated by the degradation of flumequine antibiotic (FLQ) in a UV reactor. There was no remarkable difference between the results obtained from pure MgO and La-doped MgO when the photo-degradation was performed in the dark. Blank experiments were also carried out under UV light in the absence of any catalyst. The antibiotic degradation yield was very low, confirming that light irradiation alone is not sufficient for the degradation of FLQ. The characteristic absorption peak of FLQ (λ_{max} 248 nm) was used to monitor the degradation yield. An FLQ stock solution (10 mg/L) was freshly prepared, out of which, 50 mL portions and 0.1 g of catalyst were transferred into the UV reactor. The mixture was stirred for 60 min in the dark to obtain adsorption/desorption equilibrium. The data provided in Fig. 7b were used to calculate the apparent rate constants (k_{app}) for different catalysts. A pseudo-first-order equation was used to explain the kinetics of the FLQ photocatalytic degradation. The first-order kinetic rate k (1/min) for FLQ degradation can be calculated by plotting $\ln\frac{C_0}{C}$ versus time (t). At 30 min intervals, 1 mL of sample was withdrawn and filtered to monitor degradation rates. The % degradation of FLQ was calculated using Eq. 5:

$$\%\text{Degradation} = \frac{C_0 - C}{C_0} \times 100 = \frac{A_0 - A_t}{A_t} \times 100 \quad (5)$$

where A_0 and A_t are the initial and final absorbencies of FLQ at 248 nm. According to the Beer-Lambert law, initial and final absorbencies represent the initial (C_0) and final (C) concentrations of the analyte i.e. FLQ.[32]

Figure 6a and b present the photocatalytic degradation yield of pure MgO and La-doped MgO samples. Pure MgO displayed very low degradation efficiency due to the higher band gap value. Furthermore, pure MgO and La-doped MgO showed differential catalytic performance according to the following order: 4La-MgO > 2La-MgO > 6La-MgO > 1La-MgO > MgO. The 4La-MgO sample showed higher catalytic activity than the other samples, which is probably due to the greater number of surface defects observed by PL. Also, a certain concentration of La^{+3} in the MgO structure can inhibit the recombination of the charged species. Additionally, the doped lanthanum ions act as shallow electron-trapping centers, which leads to high photocatalytic performance.[33] Therefore, the highest photocatalytic activity was

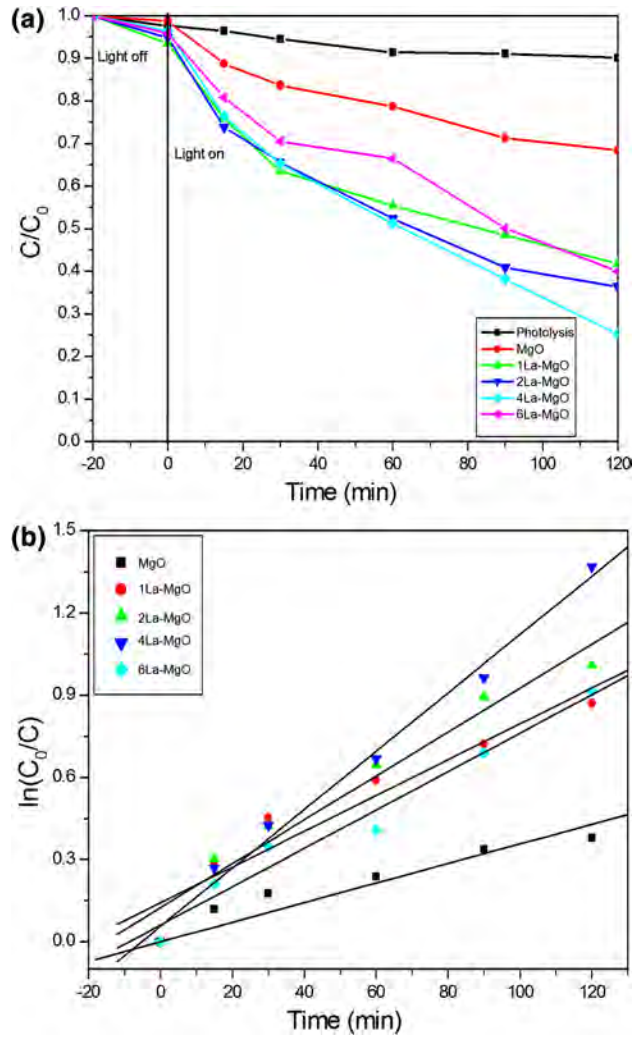

Fig. 6. The comparison of the degradation rate of pure MgO and La-doped MgO samples (a), the pseudo-first-order kinetic rate constant and regression for the pure MgO and La-doped MgO (b).

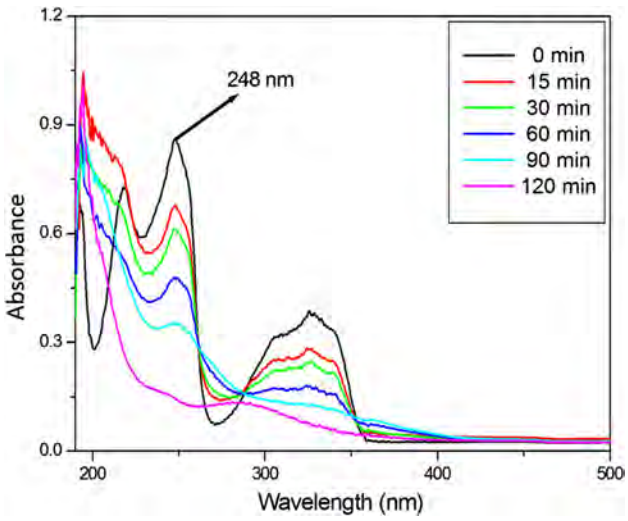

Fig. 7. UV-Vis spectra of FLQ degradation at different time intervals.

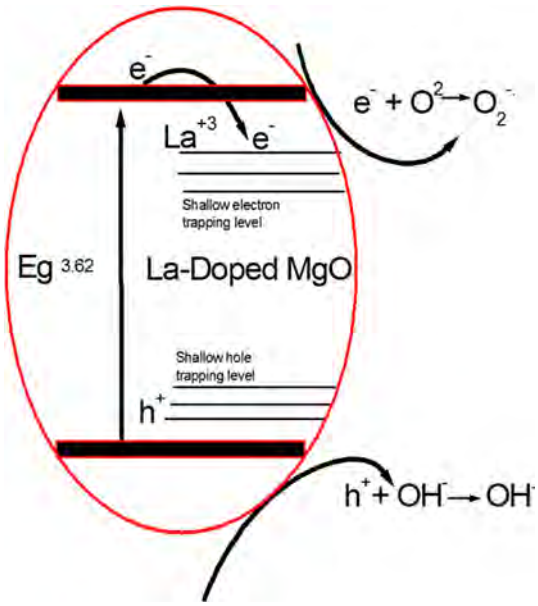

Fig. 8. Schematic illustration of the mechanism of degradation catalyzed by La-doped MgO.

obtained when 4La-MgO was used. On the other hand, the photocatalytic activity did not increase when an excess of La was used. This result may be explained by the fact that: (I) higher La content can occupy most of the MgO surface and reduce the naked area exposed to UV irradiation. Thus lower photocatalytic activity was obtained; (II) excess La doped onto MgO can serve as a recombination center.

Figure 7 shows the absorption spectra of FLQ at different irradiation times. The intensity of the characteristic absorption peak of FLQ at 248 nm decreased as the time passed. This confirms the efficient FLQ degradation by 4La-MgO.

Figure 8 shows the degradation mechanism. The band gap of La^{3+}-doped MgO is narrower (3.62 eV) than that of pure MgO (3.88 eV), suggesting greater UV light absorption by La-MgO, and thereby facilitating the production of electrons and holes. When La-doped MgO was irradiated with UV light, the VB electrons of MgO were excited to the CB level. The excited electrons transferred to the shallow trapping level due to the La^{+3}. These combined processes can separate the electron–hole pairs that play a significant role in the degradation process. The obtained degradation results and band gap value were compared with the other La-doped photocatalysts (Table II). The band gap of the photocatalysts shifted towards the visible light region upon doping with La^{+3}. This situation is useful for a visible light photocatalyst. Although the La-doped MgO has higher band gap energy, it performed efficient FLQ removal compared to the other reports (Table II). Unlike other studies, in addition to the band gap value, the formation of the second phase, as observed in the case of La_2O_3 during the present study, played an active role in the degradation.

CONCLUSIONS

A series of La-doped MgO samples with different La^{+3} concentrations (1%, 2%, 4% and 6%) were successfully prepared and characterized by SEM, TEM, XRD, XPS, PL and UV–vis analyses. The obtained results showed that La^{3+} ions doped in MgO are more effective. The UV–vis spectra of La-

Table II. Comparison of the photocatalytic performance of some La-doped catalysts

Photocatalyst	Band gap (eV)	Degradation yield	Sample pollutant	References
La-doped MgO	3.62	78	Flumequine	This study
La-doped ZnO	2.94	99	Paracetamol	Ref. 19
La-doped BiOBr	2.59	48	Ciprofloxacin	Ref. 33
La-doped $BiFeO_3$	2.06	96	Phenol	Ref. 34
La-doped TiO_2	2.39	94	Acid Green 25	Ref. 35

doped MgO were redshifted due to the secondary La_2O_3 phase. The effect of La^{+3} in the MgO structure on the degradation of the antibiotic FLQ was also investigated. The 4La-MgO sample was more active than the other photocatalysts under UV light.

ACKNOWLEDGEMENT

This study has been supported by Mugla Sitki Kocman University Coordination of Scientific Research with Project Number 15/139.

REFERENCES

1. N.J. Naghashkar, M.G. El-Din, and K. Ikehata, *Ozone, Sci. Eng.* 28, 353 (2007).
2. T.A. Ternes, *Water Res.* 32, 3245 (1998).
3. P.S.M. Dunlop, M. Ciavola, L. Rizzo, D.A. McDowell, and J.A. Byrne, *Cat. Today* 240, 55 (2015).
4. K. Kus'mierek, *React. Kinet. Mech. Cat.* 119, 19 (2016).
5. F.M. Diogo Santos, O.S.G.P. Soares, A.M.T. Silva, J.L. Figueiredo, and M.F.R. Pereira, *Appl. Catal. B-Environ.* 199, 361 (2016).
6. Y.X. Wang, A. Zhimin, H.Q. Sun, X.G. Duan, and S.B. Wang, *Appl. Catal. B-Environ.* 198, 295 (2016).
7. G.S. Pozan, M. Isleyen, and S. Gokcen, *Appl. Catal. B-Environ.* 140, 537 (2013).
8. C. Hai, Y. Zhou, Y. Du, Y. Sun, J. Zeng, Y. Shen, and O. Dong, *Mater. Res. Bull.* 85, 181 (2017).
9. X.W. Sun, Z.J. Liu, Q.F. Chen, W.L. Quan, Z.G. Chen, and Y.H. Li, *Mater. Res. Bull.* 44, 1729 (2009).
10. M.P.G. Mantilaka, R.T. De Silva, S.P. Ratnayake, G. Amaratunga, and K.N. de Silva, *Mater. Res. Bull.* 99, 204 (2018).
11. M.M.G.P.G. Mantilaka, H.M.T.G.A. Pitawala, D.G.G.P. Karunaratne, and R.M.G. Rajapakse, *Colloid Surface A* 443, 201 (2014).
12. M.H. Bartl, K.L. Frindell, M.R. Robinson, G.C. Bazan, A. Popitsch, and G.D. Stucky, *J. Solid State Chem.* 172, 81 (2003).
13. A. Zhu, X. Zhang, X. Li, and W. Gong, *Catal. Today* 89, 97 (2004).
14. J. Yang, J. Lang, L. Yang, Y. Zhang, D. Wang, H. Fan, H. Liu, Y. Wang, and M. Gao, *J Alloys Compd.* 450, 521 (2008).
15. A.N. Banerjee, N. Hamnabard, and S.W. Joo, *Ceram. Int.* 42, 12010 (2016).
16. A. Najafi, *Ceram. Int.* 43, 5813 (2017).
17. C. Manoharan, M. Jothibas, S.J. Jeyakumar, and S. Dhanapandian, *Spectrochim Acta Part A Mol Biomol. Spectrosc.* 145, 47 (2015).
18. G. Varughese, K.T. Usha, and A.S. Kumar, *IJLRST* 3, 133 (2014).
19. V.H.T. Thi and B.K. Lee, *Mater. Res. Bull.* 96, 171 (2017).
20. K.P. Priyanka, V.R. Revathy, P. Rosmin, B. Thrivedu, K.M. Elsa, J. Nimmymol, and T. Varghese, *Mater. Charac.* 113, 144 (2016).
21. C. Jin, H. Kim, S. An, and C. Lee, *Chem. Eng. J.* 198, 420 (2012).
22. K. Mageshwari, S.S. Mali, R. Sathyamoorthy, and P.S. Patil, *Powd. Technol.* 249, 456 (2013).
23. H.W. Kim and S.H. Shim, *Chem. Physics Lett.* 422, 165 (2006).
24. K. Kodama and T. Uchino, *J. Appl. Phys.* 111, 093525 (2012).
25. M.A. Kumar, H.P. Nagaswarupa, S.C. Prashantha, K. Channakeshavalu, K.S. Anantharaju, H. Nagabhushana, and K.V. Mahesh, *Mater. Today Proc.* 4, 11737 (2017).
26. A.L. Gajengi, T. Sasaki, and B.M. Bhanage, *Adv. Powd. Technol.* 28, 1185 (2017).
27. B.A. Taleatu, E. Omotoso, C. Lal, W.O. Makinde, K.T. Ogundele, E. Ajenifuja, and G.T. Mola, *Surf. Int. Anal.* 46, 372 (2014).
28. Y. Rao, W. Wang, F. Tan, Y. Cai, J. Lu, and X. Qiao, *Ceram. Int.* 40, 14397 (2014).
29. M. Jothibas, C. Manoharan, S.J. Jeyakumar, P. Praveen, I.K. Punithavathy, and J.P. Richard, *Sol. Energy* 159, 434 (2018).
30. A.I. Vaizoğullar, *Chem. Eng. Commun.* 204, 695 (2017).
31. S. Suwanboon, S. Klubnuan, N. Jantha, P. Amornpitoksuk, and P. Bangrak, *Mater. Lett.* 115, 275 (2014).
32. X.T. Gao and I.E. Wachs, *Catal. Today* 51, 233 (1999).
33. S. Yin, W. Fan, J. Di, T. Wu, J. Yan, M. He, J. Xia, and H. Li, *Colloid Surf. A* 513, 160 (2017).
34. W. Meng, R. Hu, J. Yang, Y. Du, J. Li, and H. Wang, *Chin. J. Catal.* 37, 1283 (2016).
35. W. Raza, M.M. Haque, M. Muneer, M. Fleisch, A. Hakki, and D. Bahnemann, *J. Alloy. Compd.* 632, 837 (2015).